On the nonlinear structural analysis of wind turbine blades using reduced degree-of-freedom models

K. Holm-Jørgensen[†], J.W. Stærdahl[‡] and S.R.K. Nielsen[‡†]

*Department of Civil Engineering, Aalborg University, Sohngaardsholmsvej 57,
DK-9000 Aalborg, Denmark*

Abstract. Wind turbine blades are increasing in magnitude without a proportional increase of stiffness for which reason geometrical and inertial nonlinearities become increasingly important. Often these effects are analysed using a nonlinear truncated expansion in undamped fixed base mode shapes of a blade, modelling geometrical and inertial nonlinear couplings in the fundamental flap and edge direction. The purpose of this article is to examine the applicability of such a reduced-degree-of-freedom model in predicting the nonlinear response and stability of a blade by comparison to a full model based on a nonlinear co-rotating FE formulation. By use of the reduced-degree-of-freedom model it is shown that under strong resonance excitation of the fundamental flap or edge modes, significant energy is transferred to higher modes due to parametric or nonlinear coupling terms, which influence the response and stability conditions. It is demonstrated that the response predicted by such models in some cases becomes instable or chaotic. However, as a consequence of the energy flow the stability is increased and the tendency of chaotic vibrations is reduced as the number of modes are increased. The FE model representing the case of infinitely many included modes, is shown to predict stable and ordered response for all considered parameters. Further, the analysis shows that the reduced-degree-of-freedom model of relatively low order overestimates the response near resonance peaks, which is a consequence of the small number of included modes. The qualitative erratic response and stability prediction of the reduced order models take place at frequencies slightly above normal operation. However, for normal operation of the wind turbine without resonance excitation 4 modes in the reduced-degree-of-freedom model perform acceptable.

Keywords: wind turbine blades; nonlinear vibration; bernoulli-euler beam; co-rotating finite elements; truncated modal expansion.

1. Introduction

In simulating the behaviour of a wind turbine many load combinations are studied to ensure that the wind turbine is designed to withstand throughout its lifetime. Normally, these life cycle simulations are performed using reduced-degree-of-freedom models because the computation time has to be short. The worst cases are next used in more advanced structural models to verify and optimize the design. During on-line operation of the wind turbine it is also essential with fast working models, in case of active or semi-active vibration control when such mechanisms are

---

† Ph.D. Student, Corresponding author, E-mail: khj@civil.aau.dk
‡ Assistant Professor, Ph.D., E-mail: jws@civil.aau.dk
‡† Professor, Ph.D., E-mail: soren.nielsen@civil.aau.dk

installed. In this paper the predictions of response and stability of a wind turbine blade based on such nonlinear reduced-degree-of-freedom model are validated by comparison with those of a full nonlinear co-rotating FE model. Both models are formulated in a moving frame of reference following the stiff body motion of the blade. The considered reduced-order model is based on a spatial discretization using the fixed base undamped eigenmodes as a functional basis. The model incorporates linear and nonlinear coupling terms between the different modes making energy transfer a possibility, contrary to a linear model. This energy transfer is essential for correct stability and response prediction. The geometrical nonlinear terms of the model originate from a nonlinear description of the curvature of the blade and the rotation of internal and external forces during the deformation. The inertial nonlinearities are caused by inertial axial forces induced by the support point motion. The undamped fixed base eigenmodes are determined from an FE model of a beam with pretwist using the Bernoulli-Euler beam theory with St. Venant torsion.

In Larsen and Nielsen (2006a) and Larsen and Nielsen (2006b) the two lowest modes were retained reducing the equations of motion to a nonlinear 2-degree-of-freedom system with the above-mentioned nonlinear coupling terms. The idea was to investigate 2:1 internal resonance, due to the eigenfrequency of the lowest edge mode is approximately two times the eigenfrequency of the fundamental blade mode. Among the many studies was the relative influence of the different parametric and nonparametric coupling terms along with the placement of the resonance peaks. The stability of the 2-degree-of-freedom model was studied by a numerical calculated Lyapunov exponent based on the algorithm of Wolf *et al.* (1984) for different relations between the first two eigenfrequencies and for different relations between the frequency of the support point motion and rotor rotation. At some excitation frequencies the response became both instable and chaotic. During resonance, where the influence of nonlinearities is significant and the modal equations become strongly coupled, it is questionable if only 2 modes are sufficient to get a correct prediction of the response and stability. For this reason a convergency test is performed in this paper increasing the number of modes to 4 and 6. Especially, the primarily nonlinear terms responsible for the energy transfer between the modes are identified. Finally, the response and stability of the model by 2, 4 and 6 modes are compared to a full nonlinear co-rotating FE-beam model. The idea is to investigate to which extent the energy transfer to higher modes than included in the reduced-degree-of-freedom may influence qualitatively on the response and stability predictions.

With emphasis on beam models for a rotor blade Volovoi *et al.* (2001) have reviewed several beam theories considering effects such as transverse shear flexibility, Vlasov's warping etc. The overall conclusions were that for thin-walled box sections the Bernoulli-Euler theory containing extension with St. Venant torsion and bending in two directions behaved adequately in most cases. However, for short-wavelength modes shear effects need to be included using Timoshenko theory as demonstrated by Yu *et al.* (2002). The study of flexible bodies attached to a moving support has continued over seventy years. Baker *et al.* (1993) examined the response and stability of a parametric and chaotic excited beam both experimentally and analytically. The analytical model, derived by a Galerkin reduction of the plane equations of motion, could predict the behaviour from parametric excitation but not for chaotic excitation. The slow convergence of a modal expansion can be overcome by an expansion in nonlinear modes, Nayfeh *et al.* (1995). Based on a nonlinear Bernoulli-Euler FE-beam model of a cantilever rotating beam, Apiwattanalunggarn *et al.* (2003) devised a reduced model by use of a nonlinear normal mode expansion. Excellent agreement was achieved by comparison to a full reference model. In creating a reference model the nonlinear co-rotating formulation is ideal for large displacements. In this formulation a local coordinate system

undergoing rigid body motion is assigned to each element. In this local coordinate system the elastic deformations are small whereby regular beam theory is sufficient. This method has existed since the seventies and described and examined in a number of papers and text books, among these Crisfield 1990 and Krenk 2005. The primary deviation between the formulations is the way of incorporating rotations in three dimensions, because finite rotations do not add linearly as vectors. In Sandhu *et al.* (1990) Euler rotations are used and the performance of the formulation is compared to other large deformation formulations by a number of examples using curved 3D-beam elements showing accurate and fast converging results. In the method described in Krenk (2005) quaternions are used to describe the finite rotation of the nodes from which mean rotations are introduced to determine the orientation of the base unit vectors of each element. In Crisfield *et al.* (1997) several time integration algorithms using 3D co-rotational beams with two nodes and six degrees of freedom per node are examined showing good performance by including numerical damping. Other authors observed good experience by use of the Newmark integration with Newton Raphson iteration for a co-rotational finite element formulation, e.g., Hsiao *et al.* (1999) and Behdinan *et al.* (1998).

In a regular three-bladed wind turbine the relation between the excitation frequency and the rotational frequency of the rotor is $\omega_0/\Omega_0 = 3$ due to changes in wind load when the individual blades are in top and bottom positions of the incoming shear wind field. This is an idealized ratio as turbulence will introduce other ratios. Moreover, the relation between the excitation frequency and the first eigenfrequency of the blade is below 1 i.e., $\omega_0/\omega_1 < 1$ during normal operation. In the following simulations the response and stability will be examined for a frequency band of $\omega_0/\omega_1 \in [0.5;1.5]$ well knowing that this interval is above the normal operating values of a wind turbine. However, this larger interval will prove if the model produces stable results and examine what happens in case of failure e.g., where the rotor speeds up. The chosen interval will result in rotational frequencies of $\Omega_0 \in [0.77;2.31]$rad/s where the nominal value is $\Omega_0 = 1.6$ rad/s. In Larsen and Nielsen (2006a) the first fixed base eigenfrequency of the blade at the nominal rotational frequency of the rotor is $\omega_1 = 5.14$ rad/s resulting in a non-dimensional excitation frequency of $\omega_0/\omega_1 = 0.93$ for normal operation. A shell model of the blade has been created giving the 10 lowest eigenmodes i.e. up to a eigenfrequency of $\omega_{10} = 111.31$ rad/s. The eigenfrequency corresponding to the first torsional mode is $\omega_9 = 100.22$ rad/s, which does not have any significant bending components. Also the remaining considered modes do not show any significant coupling between bending and torsional components. Therefore, the torsional degree-of-freedom and eventually couplings with bending components are not included in the model.

2. Reduced degree-of-freedom model

In this section the reduced degrees-of-freedom model is introduced together with the main expressions, ending up with the nonlinear equations of motion for the modal coordinates. The section is based on Larsen and Nielsen (2006a) where a more detailed description of the model and the derived equations of motion can be found.

2.1 Coordinate systems and support point motions

In Fig. 1(a) the wind turbine is seen from upwind where the rotor rotates in the clockwise direction. A fixed global (x_1, x_2, x_3)-coordinate system is placed at the ground level in the centre of
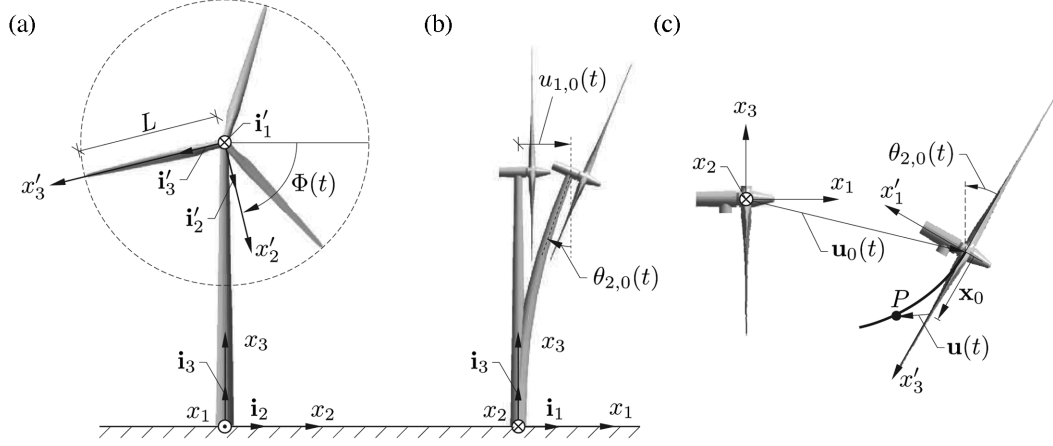
Fig. 1 (a) Wind turbine seen from upwind, (b) Displacement of the nacelle, (c) Displacement of a material point in the blade

the tower. The x_1-axis is oriented parallel to the rotor axes as shown in Fig. 1. To simplify the matter it is assumed that the nacelle is not tilted and the blades are not coned. The length of a blade is denoted L. A local (x_1', x_2', x_3')-coordinate system is fixed to the blade with origin at the hub with the centre of gravity of the sections placed on the x_3'-axis. The x_1'-and x_2'-axis are placed in such a way that they represent the flap-and edge-wise displacement, respectively. The position of the x_2'-axis is determined by the phase angle $\Phi(t)$ which is defined clock-wise from the global x_2-axis. The displacement and rotation of the hub, originating from the motion of the tower and nacelle, are accounted for by introducing a prescribed linear translation and rotation with the global coordinates $u_{i,0}(t)$ and $\theta_{i,0}(t)$, respectively.

In the following it is assumed that the motion of the nacelle and thereby the support point motion only take place in the (x_1, x_3)-plane, corresponding to the following components, see Fig. 1(b).

$$u_{1,0}(t) = u(t), \quad \theta_{2,0}(t) = \Theta_{2,0}u(t), \quad u_{2,0}(t) = u_{3,0}(t) = \theta_{1,0}(t) = \theta_{3,0}(t) = 0 \qquad (1)$$

Here it is assumed that the motion of the tower is controlled by a simple modal coordinate representing the horizontal motion $u(t)$ of the nacelle. $\Theta_{2,0}$ is a scaling factor for the corresponding rotation of the nacelle. In the following $u(t)$ is assumed to vary harmonically with the amplitude u_0 and excitation frequency ω_0 as

$$u(t) = u_0\cos\omega_0 t \qquad (2)$$

Let $\underline{v}'$ and $\underline{v}$ be column matrices storing the moving frame and fixed frame components of a vector $\mathbf{v}$. These components are related as

$$\underline{v}' = \underline{A}\,\underline{v} \qquad (3)$$

$\underline{A}$ represents the components of the rotation tensor, rotating the fixed frame base vectors to the moving frame base vectors, i.e., $\mathbf{i}_i' = A_{ij}\mathbf{i}_j$. The transformation matrix $\underline{A}(t)$ is found as a sequence of rotations. First, a rotation $\theta_{2,0}$ of the rotor plane around the global x_2-axis is performed, followed by

a blade rotation $\Phi(t)$ around the x_1'-axis of the blade fixed (x_1', x_2', x_3')-coordinate system.

$$\left. \begin{array}{l} \underline{v}_1 = \underline{A}_1 \underline{v} \\ \underline{v}' = \underline{A}_2 \underline{v}_1 \end{array} \right\} \Rightarrow \underline{v}' = \underline{A}_2 \underline{A}_1 \underline{v}, \quad \underline{A} = \underline{A}_2 \underline{A}_1 \tag{4}$$

where

$$\underline{A}_1(t) = \begin{bmatrix} \cos\theta_{2,0} & 0 & -\sin\theta_{2,0} \\ 0 & 1 & 0 \\ \sin\theta_{2,0} & 0 & \cos\theta_{2,0} \end{bmatrix}, \qquad \underline{A}_2(t) = \begin{bmatrix} -1 & 0 & 0 \\ 0 & \cos\Phi & -\sin\Phi \\ 0 & -\sin\Phi & -\cos\Phi \end{bmatrix} \tag{5}$$

The local components of the support point motion are $u_{i,0}'(t) = A_{i1}(t)u(t)$ and $\theta_{i,0}'(t) = A_{i2}\Theta_{2,0}u(t)$, where $A_{i1}(t)$ and $A_{i2}(t)$ denote the components in the 1st and 2nd columns of $\underline{A}(t)$.

$$\underline{u}_0'(t) = \begin{bmatrix} -\cos\theta_{2,0} \\ -\sin\Phi\sin\theta_{2,0} \\ -\cos\Phi\sin\theta_{2,0} \end{bmatrix} u(t), \qquad \underline{\theta}_0'(t) = \begin{bmatrix} 0 \\ \cos\Phi \\ -\sin\Phi \end{bmatrix} \Theta_{2,0}u(t) \tag{6}$$

To simplify matters further, the effects on the hub displacement from the rotation $\theta_{2,0}$ are disregarded. Hence, $u_{1,0}'(t) \simeq -u(t)$, $u_{2,0}'(t) = u_{3,0}'(t) \simeq 0$.

The time-derivative of $\Phi(t)$ specifies the rotational speed of the rotor

$$\Omega_0(t) = \dot{\Phi}(t) \tag{7}$$

2.2 Modal equations of motion

In order to discretize the variational equations obtained from the principles of virtual work, the displacement components $u_\alpha'(x_3', t)$ and the variational field $\delta u_\alpha'(x_3')$ are represented by the following modal expansions

$$u_\alpha'(x_3', t) \simeq \sum_{j=1}^{N} \Phi_\alpha^{(j)}(x_3')q_j(t), \quad \delta u_\alpha'(x_3', t) = \sum_{j=1}^{N} \Phi_\alpha^{(j)}(x_3')\delta q_j(t) \tag{8}$$

where $u_1'(x_3', t)$ is the deformation component in the flap direction, and $u_2'(x_3', t)$ is the deformation component in the edgewise direction. $q_j(t)$ and δq_j denote the modal coordinates and virtual variations of this quantity. $\Phi_\alpha^{(j)}(x_3')$ represents the undamped eigenmodes, where the upper index denotes the mode number and the lower index indicates the component. A discretized version of $\Phi_\alpha^{(j)}(x_3')$ has been obtained by means of an FE-method, from which all necessary derivatives of the eigenmodes also are obtained as described in Larsen and Nielsen (2006a). Retaining nonlinearities up to 3rd order the ordinary differential equations for the modal coordinates become, Larsen and Nielsen (2006a)

$$\sum_{j=1}^{N} (m_{ij}\ddot{q}_j + c_{ij}(t)\dot{q}_j + k_{ij}(t)q_j) + \sum_{j=1}^{N}\sum_{k=1}^{N} (a_{ijk}(t)q_jq_k + b_{ijk}(t)q_j\dot{q}_k)$$

$$+ \sum_{j=1}^{N}\sum_{k=1}^{N}\sum_{l=1}^{N} (d_{ijkl}q_jq_kq_l + g_{ijkl}(q_j\dot{q}_k\dot{q}_l + q_jq_k\ddot{q}_l)) = f_i(t) \tag{9}$$

where

$$m_{ij} = M_i \delta_{ij}$$

$$c_{ij}(t) = 2\zeta_i \omega_i M_i \delta_{ij} + \int_0^L \mu \Phi_\alpha^{(i)} E_{\alpha\beta} \Phi_\beta^{(j)} dx_3'$$

$$k_{ij}(t) = M_i \omega_i^2 \delta_{ij} + \int_0^L \left[\mu \Phi_\alpha^{(i)} D_{\alpha\beta} \Phi_\beta^{(j)} - \frac{\partial \Phi_\alpha^{(i)}}{\partial x_3'} \frac{\partial \Phi_\alpha^{(j)}}{\partial x_3'} \int_{x_3'}^L \mu D_{33} x_3' \, dx_3' \right] dx_3' \tag{10}$$

In Eq. (10) and below the summation convention is used on the Greek indices which count from 1 to 2, e.g., $\frac{\partial \Phi_\alpha^{(i)}}{\partial x_3'} \frac{\partial \Phi_\alpha^{(j)}}{\partial x_3'} = \frac{\partial \Phi_1^{(i)}}{\partial x_3'} \frac{\partial \Phi_1^{(j)}}{\partial x_3'} + \frac{\partial \Phi_2^{(i)}}{\partial x_3'} \frac{\partial \Phi_2^{(j)}}{\partial x_3'}$. M_i specifies the modal mass for mode i, δ_{ij} is the Kronecker's delta. ω_i signifies the eigenfrequency of mode i. $c_{ij}(t)$ denotes the components of the modal damping matrix. The first term on the right-hand side signifies the structural damping determined by the modal damping ratio ζ_i which is specified for each considered mode. As seen, the structural damping has been assumed to decouple in agreement with the well-separated eigenfrequencies and the low structural damping of the system. The last term represents the contribution from the Coriolis forces. μ is the mass per unit length, and $E_{\alpha\beta}$, denotes the components of the upper part of the spin rotational matrix $\underline{E}$ given as

$$\underline{E}(t) = 2\underline{A}(t)\underline{\dot{A}}^T(t) = 2 \begin{bmatrix} 0 & -\dot{\theta}_{3,0}' & \dot{\theta}_{2,0}' \\ \dot{\theta}_{3,0}' & 0 & -\Omega_0 \\ -\dot{\theta}_{2,0}' & \Omega_0 & 0 \end{bmatrix} \tag{11}$$

$k_{ij}(t)$ represents the components of the modal stiffness matrix. The first term on the right-hand side signifies the modal structural stiffness, whereas the second part indicates the geometrical stiffness due to centrifugal forces. $D_{\alpha\beta}$ and D_{33} denote the components in the matrix $\underline{D}$ given as

$$\underline{D}(t) = \underline{A}(t)\underline{\ddot{A}}^T(t) = - \begin{bmatrix} \dot{\theta}_{3,0}'^2 + \dot{\theta}_{2,0}'^2 & -\dot{\theta}_{2,0}'\Omega_0 + \ddot{\theta}_{3,0}' & -\dot{\theta}_{3,0}'\Omega_0 - \ddot{\theta}_{2,0}' \\ -\dot{\theta}_{2,0}'\Omega_0 - \ddot{\theta}_{3,0}' & \dot{\theta}_{3,0}'^2 + \Omega_0^2 & -\dot{\theta}_{3,0}'\dot{\theta}_{2,0}' + \dot{\Omega}_0 \\ -\dot{\theta}_{3,0}'\Omega_0 + \ddot{\theta}_{2,0}' & -\dot{\theta}_{3,0}'\dot{\theta}_{2,0}' - \dot{\Omega}_0 & \dot{\theta}_{2,0}'^2 + \Omega_0^2 \end{bmatrix} \tag{12}$$

The position vector of a material point from the origin of the moving frame of reference is denoted $\mathbf{x}(t) = \mathbf{x}_0(t) + \mathbf{u}(t)$, where $\mathbf{x}_0(t)$ is the undeformed or referential position and $\mathbf{u}(t)$ specifies the local displacement vector of the particle as seen by an observer fixed to the moving frame of reference, see Fig. 1(c). Then, the local components of the acceleration vector are given as, Larsen and Nielsen (2006a)

$$\underline{a}'(t) = \underline{\ddot{u}}_0'(t) + \underline{\ddot{x}}'(t) + \underline{D}(t)\underline{x}'(t) + \underline{E}(t)\underline{\dot{x}}'(t) \tag{13}$$

where $\underline{\ddot{u}}_0'(t)$ is the local components of the acceleration vector of the support point, and $\underline{x}'(t)$ stores the moving frame components of $\mathbf{x}(t)$. $\underline{D}(t)\underline{x}'(t)$ and $\underline{E}(t)\underline{\dot{x}}'(t)$ represent the local

components of the centrifugal and Coriolis accelerations, respectively. The nonlinear coupling coefficients in Eq. (9) are defined as follows

$$a_{ijk}(t) = \int_0^L \left[\frac{\partial \Phi_\alpha^{(i)}}{\partial x_3'} \frac{\partial \Phi_\alpha^{(j)}}{\partial x_3'} \int_{x_3'}^L \left[-p''_{\beta,A} \frac{\partial \Phi_\beta^{(k)}}{\partial x_3'} - \mu D_{3\beta} \Phi_\beta^{(k)} \right] dx_3' + \frac{1}{2} \Phi_\alpha^{(i)} p''_{\beta,A} \frac{\partial \Phi_\alpha^{(j)}}{\partial x_3'} \frac{\partial \Phi_\beta^{(k)}}{\partial x_3'} \right] dx_3'$$

$$b_{ijk}(t) = \int_0^L \left[\frac{\partial \Phi_\alpha^{(i)}}{\partial x_3'} \frac{\partial \Phi_\alpha^{(j)}}{\partial x_3'} \int_{x_3'}^L -\mu E_{3\beta} \Phi_\beta^{(k)} dx_3' \right] dx_3'$$

$$d_{ijkl} = \int_0^L \frac{1}{2} e_{\alpha\eta} EI''_{\alpha\beta} e_{\beta\xi} \left[\frac{\partial^2 \Phi_\eta^{(i)}}{\partial x_3'^2} \frac{\partial \Phi_\xi^{(j)}}{\partial x_3'} \frac{\partial \Phi_\gamma^{(k)}}{\partial x_3'} \frac{\partial^2 \Phi_\gamma^{(l)}}{\partial x_3'^2} + \frac{\partial^2 \Phi_\xi^{(l)}}{\partial x_3'^2} \frac{\partial \Phi_\eta^{(i)}}{\partial x_3'} \frac{\partial \Phi_\gamma^{(j)}}{\partial x_3'} \frac{\partial^2 \Phi_\gamma^{(k)}}{\partial x_3'^2} \right.$$
$$\left. + \frac{\partial^2 \Phi_\xi^{(l)}}{\partial x_3'^2} \frac{\partial \Phi_\eta^{(j)}}{\partial x_3'} \frac{\partial \Phi_\gamma^{(i)}}{\partial x_3'} \frac{\partial^2 \Phi_\gamma^{(k)}}{\partial x_3'^2} + \frac{\partial^2 \Phi_\xi^{(l)}}{\partial x_3'^2} \frac{\partial \Phi_\eta^{(j)}}{\partial x_3'} \frac{\partial \Phi_\gamma^{(k)}}{\partial x_3'} \frac{\partial^2 \Phi_\gamma^{(i)}}{\partial x_3'^2} \right] dx_3'$$

$$g_{ijkl} = \int_0^L \left[\frac{\partial \Phi_\alpha^{(i)}}{\partial x_3'} \frac{\partial \Phi_\alpha^{(j)}}{\partial x_3'} \int_{x_3'}^L \left[\mu \int_0^{x_3'} \frac{\partial \Phi_\beta^{(k)}}{\partial x_3'} \frac{\partial \Phi_\beta^{(l)}}{\partial x_3'} dx_3' \right] dx_3' \right] dx_3' \tag{14}$$

As seen, the parametric excitation from $\theta'_{2,0}(t)$ and $\theta'_{3,0}(t)$ is also present in the quadratic nonlinear coupling terms $a_{ijk}(t)$ and $b_{ijk}(t)$. The quadratic nonlinear coupling coefficient $a_{ijk}(t)$ includes both contributions from the rotation of the aeroelastic loads orthogonal to the deformed blade and inertial contributions from the support point rotations and the rotational frequency of the rotor. $b_{ijk}(t)$ is also a quadratic non-linear coupling coefficient originating from inertial nonlinearities from the support point rotation and the rotation of the rotor. $a_{ijk}(t)$ is influenced by centrifugal terms, whereas Coriolis terms enter in $b_{ijk}(t)$. The cubic coupling term d_{ijkl} is due to the nonlinear description of the curvature. E is the modulus of elasticity and $e_{\alpha\beta}$, is the permutation symbol given as

$$e_{\alpha\beta} = \begin{bmatrix} 0 & 1 \\ -1 & 0 \end{bmatrix} \tag{15}$$

$I''_{\alpha\beta}$ is the inertia tensor given by

$$I''_{\alpha\beta} = I'''_{\gamma\delta} C_{\alpha\gamma} C_{\beta\delta}$$

$$\underline{\underline{I'''}} = \begin{bmatrix} I'''_{11} & 0 \\ 0 & I'''_{22} \end{bmatrix}, \qquad \underline{\underline{C}} = \begin{bmatrix} \cos\varphi & \sin\varphi \\ -\sin\varphi & \cos\varphi \end{bmatrix} \tag{16}$$

where I'''_{11} and I'''_{22} are the principal moments of inertia, and φ is the twist angle cf. Fig. 2(b). g_{ijkl} is another cubic nonlinear coupling coefficient caused by inertial nonlinearities. These are due to the axial inertial forces which contribute to the geometrical stiffness along with the static axial force. $f_i(t)$ denotes the modal loads in the ith mode given as

$$f_i(t) = \int_0^L \Phi_\alpha^{(i)}(p''_{\alpha,A} - \mu(\ddot{u}'_{\alpha,0} + D_{\alpha3} x_3'))dx_3' \tag{17}$$

The support point displacement $u'_{1,0}(t)$ only enters the equations as an additive load term via the

modal loads $f_i(t)$. $p''_{\alpha,A}$ is the aerodynamic load described in Appendix B. The time dependent coefficients are derived in Appendix A.

3. Nonlinear co-rotating beam formulation

To determine the accuracy of the reduced-degree-of-freedom model a nonlinear co-rotating beam formulation is implemented. The model is based on Krenk (2005), where a detailed derivation of the tangent stiffness matrix is given.

The idea of a co-rotating formulation is to separate the deformation of each element into a rigid body motion i.e., a translation and rotation of each element with respect to a fixed coordinate system, and an elastic deformation within the local coordinate system fixed to the element. Because the elastic deformations are moderate linear Timoshenko beam theory is adequate. Inside the local coordinate system the beam is able to deform in the longitudinal direction, rotate around the beam axis, and may undergo bending deformations and shear deformations. No coupling between wharping and axial elongation is used i.e., only St. Venant torsion (homogeneous torsion) is used. The orientation of the local coordinate system is defined by the base unit vectors $\mathbf{i}''_1, \mathbf{i}''_2, \mathbf{i}''_3$ shown in Fig. 2(a). The x''_3-axis is chosen along the deformed beam through the end points A and B of the element, and the x''_1-and x''_2-axis are defined by the mean rotation at A and B. To get a simple approach for constructing the constitutive relations the principal axes are introduced. This is done by rotating the base unit vectors $\mathbf{i}''_1, \mathbf{i}''_2, \mathbf{i}''_3$ the angle φ around the x''_3-axis corresponding to the pretwist of the profile as shown in Fig. 2(b). The inertia of the blade is described by a constant consistent mass matrix for a 3D-beam element. The inertial loads from the support point motion together with the centrifugal and Coriolis contributions are determined from the respective acceleration terms in Eq. (13) multiplied with a lumped mass matrix. Prismatic elements are used when all geometric and material parameters are assigned. In solving the equations of motion Newton-Raphson iteration is used. For time integration a nonlinear Newmark with numerical damping has shown reliable.
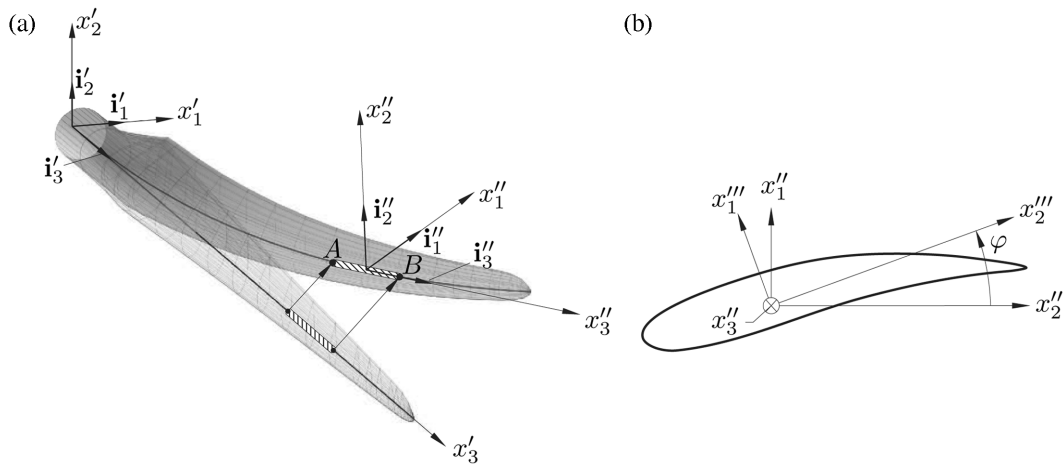

Fig. 2 (a) an element in the co-rotating formulation, (b) rotation into principal axes based on the initial pretwist of the profile and the angle to the principal axes

4. Convergency studies of the reduced-degree-of-freedom model

In this section several simulations of the reduced-degree-of-freedom model are performed with the intention to determine the number of necessary eigenmodes with respect to response and stability. Also the nonlinear couplings and related energy transfer are identified. The stability analysis is based on a numerical calculated Lyapunov exponent using the algorithm by Wolf *et al.* (1984). In the analysis the effect of including two, four and six modes is investigated.

4.1 Input parameters

As mentioned in the introduction it is chosen to fix the ratio between the support frequency and the rotational frequency of the rotor at $\omega_0/\Omega_0 = 3$. Moreover, the relation between the support frequency and the first eigenfrequency of the blade is varied in the interval $\omega_0/\omega_1 \in [0.5;1.5]$. Hence, as ω_0 is varied the rotational speed Ω_0 must change accordingly. In all the following simulations the amplitude of the horizontal displacement of the nacelle is kept at the value $u_0 = 0.3$ m. The model parameter of the rotation of the support is held constant at $\Theta_{2,0} = 0.03$ m^{-1} cf. Eq. (1). The time integration is performed by a 4th order Runge Kutta with the time step $\Delta t = \frac{1}{100}T_0$, where $T_0 = \frac{2\pi}{\omega_0}$. Stabilities such as variances and the Lyapunov exponent are based on time series of the length of 1000 periods. The results will be presented as the root-mean-square (RMS) value of the modal coordinates for the last fifth of the simulated time series in order to have received stationarity of the response. All initial values of the modal coordinates have been chosen to zero.

4.2 Fixed base eigenmodes of the blade

The geometrical and material parameters for the used blade are described in Appendix C. Hereby, an FE Bernoulli-Euler beam model including St. Venant torsion has been devised from which the undamped fixed base eigenmodes are determined. In Fig. 3 the flap component $\Phi_1^{(i)}$ and the edge-wise componet $\Phi_2^{(i)}$ for the first six fixed base undamped eigenmodes are illustrated with the dominating components normalized to 1 at the blade tip. Modal parameters and information regarding the shape of the eigenmodes are listed in Table 1 for the first six modes. These modes are determined from no rotational speed i.e., $\Omega_0 = 0$ whereby no additional stiffness from centrifugal contributions are added in the modes. The damping ratio for all modes is kept constant at $\zeta_j = 0.01$. In the fundamental blade mode the aerodynamic damping ratio may vary from about 0.2 in case of fully attached flow to negative values under deep stall conditions. In the used load model no aerodynamic damping is included. The result of varying ζ_1 has been examined in Larsen and

Table 1 Modal parameters for the first six fixed base eigenmodes

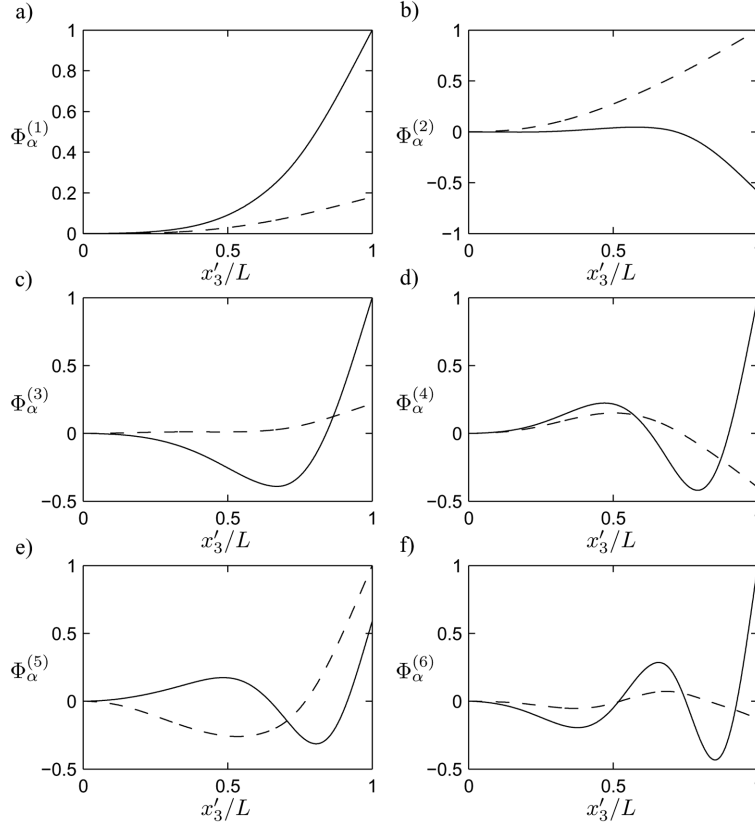| Mode $\Phi^{(j)}$	1	2	3	4	5	6
ω_j [rad/s]	4.61	9.38	13.65	29.27	34.36	52.57
M_j [kg]	399.1	846.2	367.9	326.6	471.3	232.3
Dominating component	Φ_1	Φ_2	Φ_1	Φ_1	Φ_2	Φ_1
Internal nodes in $\Phi_1^{(i)}$	0	1	1	2	2	3
Internal nodes in $\Phi_2^{(j)}$	0	0	0	1	1	2

Fig. 3 First six eigenmodes normalised to 1 in the blade tip based on the dominating component. (——) flap component, $\Phi_1^{(i)}$. (— —) edgewise component, $\Phi_2^{(i)}$

Nielsen (2006a), where the magnitude of the response at the most dominating resonance peaks approximately became one third by increasing ζ_1 from $\zeta_1 = 0.01$ to $\zeta_1 = 0.05$ and maintaining $\zeta_2 = 0.01$.

As seen in Table 1 $\omega_2 \sim 2\omega_1$, which make internal resonances between these modes possible, either due to nonlinear or parametric linear couplings between the 1st and 2nd modes.

4.3 RMS-values of the modal coordinates for different number of modes

In this section results are presented in terms of the RMS-values of the modal coordinates $q_j(t)$ as the number of modes is increased in the model. The RMS-value Q_j is defined by

$$Q_j = \left(\frac{2}{T} \int_0^T (q_j - \mu_{q_j})^2 \, dt \right)^{1/2}, \quad \mu_{q_j} = \frac{1}{T} \int_0^T q_j(t) \, dt \tag{18}$$

where μ_{q_j} is the mean value and the sampling is performed over the last $T = 200$ periods of the simulation. In Fig. 4 Q_j is plotted as a function of the nondimensional excitation frequency ω_0/ω_1 for $N = 2, 4, 6$. Since the modal functions have been normalized to one at the tip in the dominating component, Q_j may be interpreted physically as the RMS displacement at the tip in that component.

The results for Q_1, Q_3, Q_4, Q_6 and Q_2, Q_5 are plotted with different scales with respect to the flap and edge component, respectively. Two conspicuous peaks are visible in almost all modal coordinates at $\omega_0/\omega_1 \approx 0.85$ and $\omega_0/\omega_1 \approx 1.22$. As seen from Eq. (19), the modal loads $f_1(t)$ and $f_2(t)$ contain harmonic components with the circular frequencies $m\Omega_0$, $m = 1, \ldots, 4$. In combination to the frequency ratios $\omega_2 \simeq 2\omega_1$ and $\omega_0/\Omega_0 = 3$, it was shown in Larsen and Nielsen (2006b) that resonance from the load terms or internal resonance caused by linear or nonlinear parametric coupling terms may occur in the fundamental blade or edgewise modes at any of the frequency ratios $\omega_0/\omega_1 = 3/m$ and $\omega_0/\omega_1 = 6/m$, respectively, where $m = 1, \ldots, 12$. The most severe resonance
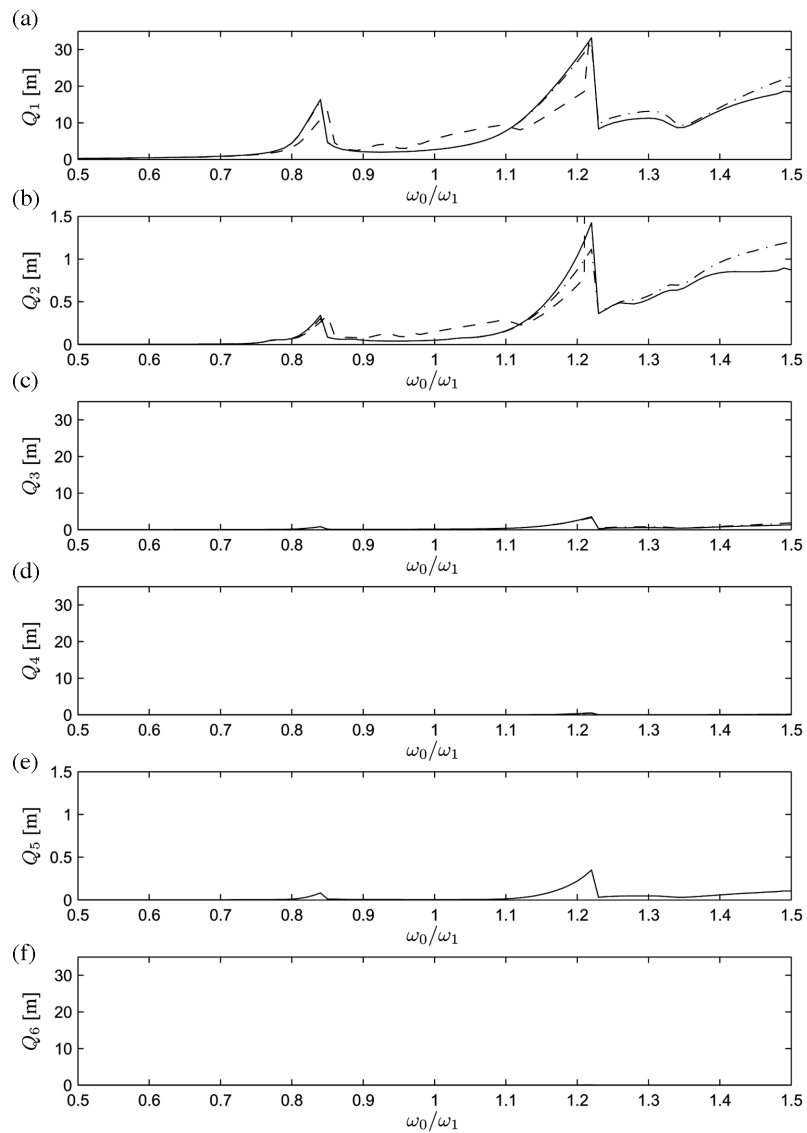

Fig. 4 RMS-values for the modal coordinates with 2, 4 and 6 modes. (– –) 2 modes. (–·–·) 4 modes. (——) 6 modes

peaks occur nearby $\omega_0/\omega_1 \simeq 3/4$ and $\omega_0/\omega_1 \simeq 1.0$ corresponding to $m = 4, 6$. In Fig. 4 the corresponding results have been shown for the present system. As seen, the peeks are placed at somewhat higher frequencies due to the geometrical stiffness from the centrifugal force, which is not introduced in the linear eigenvalue problem for finding the eigenmodes and eigenfrequencies i.e. the geometric stiffness is not included in ω_1. In Larsen and Nielsen (2006b) this effect was introduced as an additional constant term in the linear eigenvalue problem for finding the eigenmodes and eigenfrequencies. The magnitude of especially Q_1 at the resonance frequency ratio $\omega_0/\omega_1 \approx 1.22$ shown in Fig. 4(a), is high above any realistic value as the length of the blade is only 46 m. These results should merely be considered as model predictions caused by nearby instability due to loss of damping or stiffness. In reality the wind turbine will be controlled out of this region. For $N = 2$ the first peak at $\omega_0/\omega_1 \approx 0.85$ is visible in both Fig. 4(a) and Fig. 4(b). At the second peak the response becomes instable in both modal coordinates and blows up. For $N = 4$ the first peak is slightly displaced to the left in both Fig. 4(a) and Fig. 4(b), and the next peak at $\omega_0/\omega_1 \approx$ 1.22 is now visible. For $\omega_0/\omega_1 > 1.22$ the response stays inside the chosen limits, which is due to energy transfer to especially mode 3. For $N = 6$ the same characteristics as for $N = 4$ are observed, but with a slightly higher peak at $\omega_0/\omega_1 \approx 1.22$ due to resonance in mode 5, see Fig. 4(b). Both mode 4 and mode 6 contribute insignificantly to the response at all frequencies.

4.4 Stability and chaotic behaviour of the reduced-degree-of freedom model

In this section the stability and chaotic behaviour of the response will be further examined by increasing the number of included modes. The stability of the system is investigated by the largest Lyapunov exponent λ.
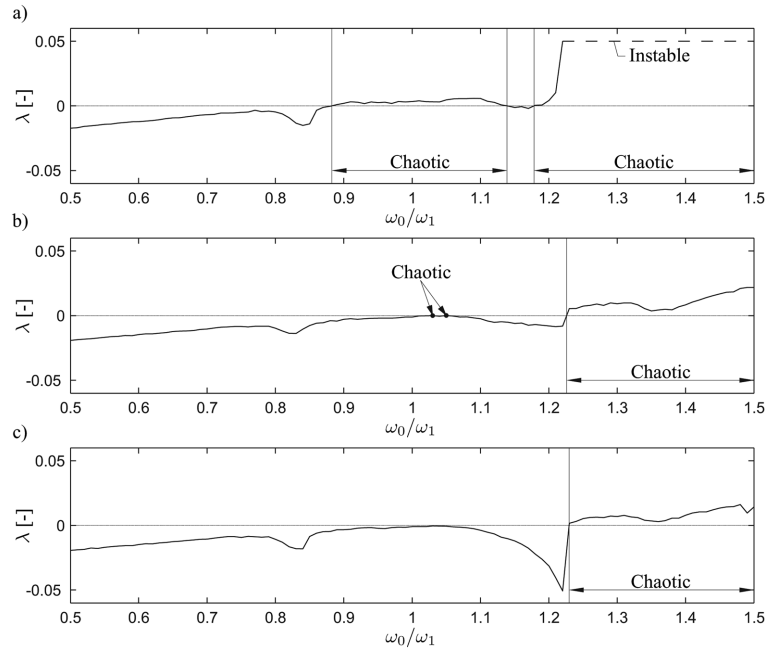

Fig. 5 Largest Lyapunov exponent with a marking of areas with chaotic response. (a) $N = 2$, (b) $N = 4$, (c) $N = 6$. (– –) Instable i.e. infinite response

In Fig. 5 the Lyapunov exponent λ has been plotted as a function of the non-dimensional excitation frequency ω_0/ω_1 for $N = 2, 4, 6$. A positive Lyapunov exponent may either indicate that the response becomes instable or chaotic i.e., that exponential growth takes place of the distance between two neighbouring states of the dynamic system in the phase space. In the following an instable response is defined as a response with infinite magnitude, whereas a chaotic response is finite but not periodic. For $N = 2$ the response is chaotic in the intervals $\omega_0/\omega_1 \approx [0.88;1.14]$, and for $\omega_0/\omega_1 > 1.18$. For $\omega_0/\omega_1 > 1.22$ the response becomes instable as also shown in Fig. 4(a) and Fig. 4(b). On Fig. 5(b) it is seen that by increasing the number of modes to $N = 4$ chaotic response is registered in small intervals around the values $\omega_0/\omega_1 = 1.03$ and $\omega_0/\omega_1 = 1.05$. For $\omega_0/\omega_1 > 1.22$ the response is chaotic but finite, cf. Fig. 4. For $N = 6$ the value of the Lyapunov exponent is further decreased and the chaotic response only takes place for $\omega_0/\omega_1 > 1.22$. Hereby, it can be concluded that the stability overall is increased, and the tendency for chaotic behaviour is reduced, as the number of included modes is increased. Based on the simulations it is evident that more than 2 modes are used. The analyses show that using 4 modes result in a good prediction of the response and stability compared with the situation where 6 modes are included. Hence, the following analyses are restricted to $N = 4$.

4.5 Coupling and energy transfer between lower and higher modes

In this section the important coupling coefficients responsible for the energy transfer between the modes are identified. The following analyses are restricted to $N = 4$ with focus on the energy transfer between the two first modes and the two next modes.

4.5.1 Dominating terms

In the following simulations it is shown that energy transfer between the two lowest modes and two next primarily takes place for $\omega_0/\omega_1 > 1.0$, where the quadratic coupling terms i.e., $a_{ijk}(t)$ and $b_{ijk}(t)$ are shown to be the most important. In these coupling terms the gyroscopic components $D_{3\beta}(t)$ and $E_{3\beta}(t)$ enter, which consist of the rotational speed of the rotor Ω_0 together with different rotation components of the support point. As ω_0/ω_1 increases so does the rotational speed of the rotor Ω_0 and the frequency of the support point displacement, whereby the coupling terms including these parameters, quite reasonable become important. The cubic coupling coefficients are both time independent and independent of the gyroscopic components whereby they have little influence on the energy transfer.

4.5.2 Energy transfer by exclusion of coupling terms

In Fig. 6 the response for Q_1 is presented for the reduced model with $N = 4$. The idea is to investigate the energy between the two lowest and the two highest modes within the model by excluding in turn linear, quadratic, and cubic coupling terms between the said modes. In Fig. 6(a) the linear coupling term i.e., the coupling coefficients m_{ij}, c_{ij} and k_{ij}, where $i = 1, 2$ and $j = 3, 4$ or $i = 3, 4$, $j = 1, 2$ are set to 0. As seen the response has only increased slightly from the full model i.e., only a small part of energy is transferred through these coupling terms and mainly at high values of ω_0/ω_1. In Fig. 6(b) the quadratic coupling coefficients $a_{ijk}(t)$ between the two lowest and two highest modes are excluded. As seen the response increases heavily at the peak $\omega_0/\omega_1 \approx 1.22$ from which is concluded that these coefficients carry a substantial flow of energy. For $\omega_0/\omega_1 > 1.22$ the response corresponds more to the full model. Fig. 6(c) shows the corresponding results where
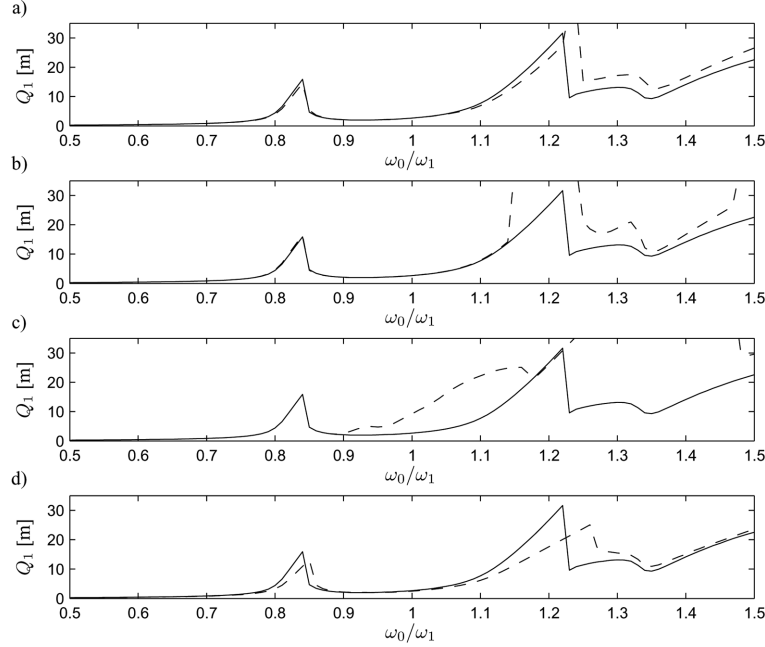
Fig. 6 Q_1 for the reduced-order-model with $N = 4$ where coupling coefficients between the two lowest and two highest modes are excluded, (a) Exclusion of linear coupling terms, (b) Exclusion of quadratic couplings in $a_{ijk}(t)$, (c) Exclusion of quadratic couplings in $b_{ijkl}(t)$, (d) Exclusion of cubic coupling terms. (——) Reduced-order-model. (– –) Exclusion of coupling coefficients

the quadratic coupling coefficients $b_{ijk}(t)$ are excluded. A large deviation relative to the reference model is registered between $\omega_0/\omega_1 \approx [0.90;1.18]$, which to some extent corresponds to the results for $N = 2$ in Fig. 4(a), but with higher RMS-values. At the peak $\omega_0/\omega_1 \approx 1.22$ only insignificant deviation is observed. However, for $\omega_0/\omega_1 > 1.22$ the response increases fast and passes out of the plot, and only enters the limits in the end. Similar, the cubic coupling coefficients only change the response minor cf. Fig. 6(d) and in this case lower the response compared to the full model. Therefore, the cubic coupling coefficients d_{ijkl} and g_{ijkl} originating from geometric and inertial nonlinearities are not the primary terms for energy transfer. From the analysis it is concluded that energy transfer primarily takes place through the quadratic coupling coefficients, where the couplings in $a_{ijk}(t)$ mainly influence the response at the peak $\omega_0/\omega_1 \approx 1.22$ and the couplings in $b_{ijk}(t)$ in the remaining part of the frequency band.

5. Comparison of the reduced-degree-of-freedom model and the co-rotating model

In this section the reduced-degree-of-freedom model with $N = 2, 4, 6$ is tested up against the nonlinear co-rotating FE-model for static and dynamic loads. The same input parameters as previous are used except that a time series with a sampling interval of 200 periods is used. A numerical damping parameter of $\alpha = 0.05$ is used in the nonlinear Newmark time integration scheme. In the co-rotating model 20 beam elements are used corresponding to 126 degrees-of-freedom. The main objectives are to compare the response and stability of the two models.

Table 2 Comparison of tip displacement between the reduced-degree-of-freedom models and the co-rotating FE-model

Model	2 modes	4 modes	6 modes	FE-model
Flap displacement [m]	5.54	5.42	5.42	5.45
Edge displacement [m]	0.86	0.83	0.82	0.80

5.1 Static load

In the first comparison a static modal load corresponding to $f_i = f_{i,00}$ in Eq. (25) is applied, where the support point is fixed and the rotor does not rotate i.e. the test corresponds to a cantilever blade. In the reduced model all included modal coordinates and their belonging mode shapes are used to determine the displacements. In Table 2 the tip displacement in the flap and edge direction for different number of included modes is compared to the corresponding results for the co-rotating FE-model.

As demonstrated previously, only small differences appear between 4 and 6 modes and the results in all cases are close to the predictions of the co-rotating FE-model. Even the results using merely 2 modes are in acceptable agreement with the referential results. It can hereby be concluded that the two models perform almost identical for a static load when 4 modes are used in the reduced-degree-of-freedom model.

5.2 Dynamic load

In this section the RMS-value of the tip displacement in the flap and edge direction is compared for the reduced order model with $N = 4$ and the FE-model. The dynamic excitation is caused by a harmonically varying support point motion in combination with a rotating rotor and aerodynamic load as in the previous investigations. In Fig. 7 the results have been given for the following interval of excitation frequencies $\omega_0/\omega_1 = [0.5;1.5]$
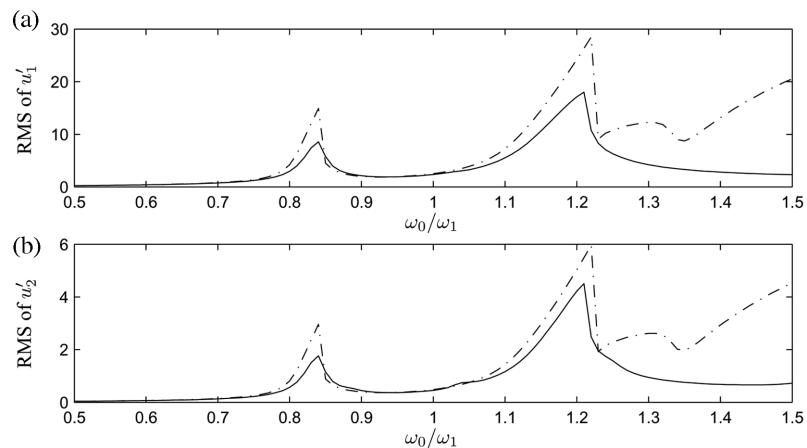

Fig. 7 RMS-values for the tip displacement in the flap and edge direction. (—·—·) 4 modes included in the reduced-degree-of-freedom model. (——) Co-rotating FE-model

As seen, the results are qualitatively in agreement for $\omega_0/\omega_1 < 1.23$, although substantial deviations appear at the resonance peaks at $\omega_0/\omega_1 \approx 0.84$ and $\omega_0/\omega_1 \approx 1.22$, where the FE-model produces much smaller response. The characteristics of the to models for $\omega_0/\omega_1 > 1.23$ are no longer similar which is due to chaotic behaviour of the reduced-degree-of-freedom model as shown in Fig. 5(b). It can hereby be concluded that the reduced-degree-of-freedom model is not valid for $\omega_0/\omega_1 > 1.23$ and it predicts too high RMS-values at the resonance peaks.

5.3 Stability

From Fig. 5 it is seen that $\omega_0/\omega_1 = 0.5$ results in stable response for all three numbers of modes, and that $\omega_0/\omega_1 = 0.9$ results in chaotic response, when 2 modes are used, and ordered response for 4 and 6 modes. For $\omega_0/\omega_1 = 1.3$ a chaotic response is obtained in all cases, and even instability for $N = 2$. These frequency ratios are used in the following stability analysis. In Fig. 8 a Poincaré map is shown for corresponding values of the tip displacement and velocity in the flap direction at time intervals $2\pi/\omega_0$ for both the co-rotating FE-model and the reduced-degree-of-freedom model for $N = 4$. It turns out that the response period is determined from the interference of the response caused by the circular frequencies $\omega_0 + \Omega_0$ and $\omega_0 - \Omega_0$, and for a rational value of $\omega_0/\Omega_0 = 3$ the response period is in Larsen and Nielsen (2006b) shown to be periodic with the period $3T_0$. For the co-rotating FE-model cf. the first row in Fig. 8, the Poincaré map shows as predicted three different points in the phase plane. This is the case for all three values of ω_0/ω_1 corresponding to an ordered response. As predicted by the Lyapunov exponent the reduced-degree-of-freedom model is stable at $\omega_0/\omega_1 = 0.5$, cf. row two in Fig. 8. For $\omega_0/\omega_1 = 0.9$ the response is ordered but with slightly more displacements of the points, and at $\omega_0/\omega_1 = 1.3$ the response is chaotic. The reduced-degree-of-freedommodel predicts chaotic response at $\omega_0/\omega_1 = 1.3$ for $N = 2, 4, 6$, which is not the case for a full model. This is due to increased transfer of energy to higher modes for the full model.
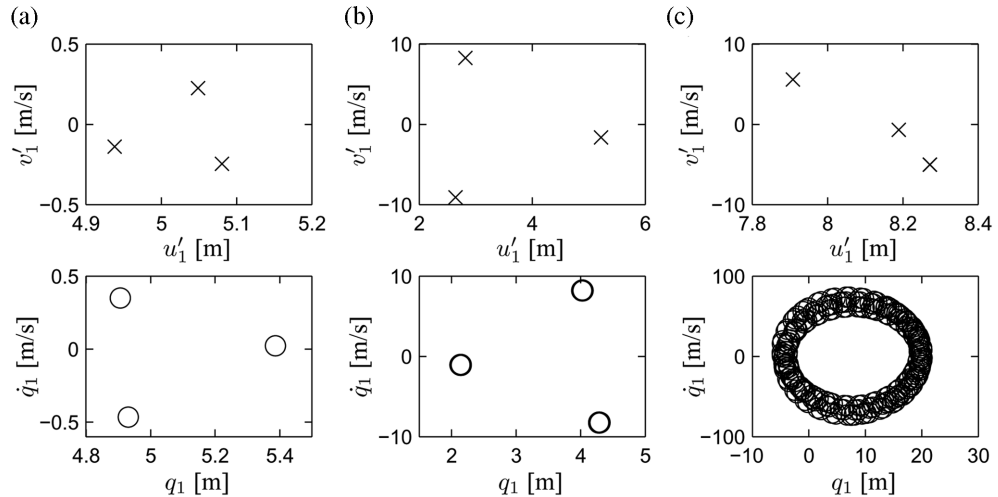

Fig. 8 Poincaré maps for tip motion in flap direction. Column (a) $\omega_0/\omega_1 = 0.5$. Column (b) $\omega_0/\omega_1 = 0.9$. Column (c) $\omega_0/\omega_1 = 1.3$

Table 3 Comparison of average computation time per period for the reduced-degreeof-freedom model and the co-rotating model

Model	2 modes	4 modes	6 modes	Co-rotating
Time/period [sek]	0.002	0.008	0.022	2.185

5.4 Time consumption

In this section the computation time of the reduced-degree-of-freedommodel and the co-rotating FE-model are compared. Both programs are developed in Fortran and in Table 3 the average simulation time per period is presented.

It is clear that even though the programs could be optimized further a major advantage is gained by using the reduced-degree-of-freedom models over the co-rotating model. From the reduced-degree-of-freedom models the time consumption increases heavily by increasing the number of modes. For large simulations it is therefore necessary to determine the minimum number of modes which produce acceptable results. Based on the previous simulations 4 modes are the best choice among the used number of modes.

6. Conclusions

Based on the convergency test of the reduced-degree-of-freedom model it can be concluded that the response by use of two modes does not deviate much from the results by including more modes when looking at a normal operating relation between the frequency of the support point motion and the first blade eigenfrequency. By comparing the results using four modes with the results using six modes almost no difference appears for $\omega_0/\omega_1 < 1$. It can also be concluded that the fourth mode contributes very little whereby three modes would result in an efficient and qualitative prediction of the response. If the system by malfunction speeds up the rotor resulting in a relation of $\omega_0/\omega_1 > 1$ it is shown that the response for two modes becomes instable, which is not the case for four modes. Including six modes do not change the qualitatively and quantitatively behaviour of the system.

From the stability analysis it is shown that by increasing the number of modes the stability of the system is improved. It is also demonstrated that the main terms for energy transfer between the first two modes and the next two are the quadratic terms which describe inertial nonlinearties from the support point motion and the rotor rotation.

In the comparison between the reduced-degree-of-freedom model and the co-rotating FE-model almost identical results under normal operation except at the resonance peaks were produced if the number of modes are four or above. This outcome was repeated both in the static, dynamic and stability tests where four modes produced results close to the co-rotating FE-model. However, for values of ω_0/ω_1 outside the normal operating area the reduced-degree-of-freedom model no longer match the co-rotating FE-model in neither response nor stability. A comparison between the time consumption for the two models showed a major gain in using the reduced-degree-of-freedom model.

It can hereby be concluded that the reduced-degree-of-freedom model is not reliable in predicting the response nor the stability for arbitrary relations between the support point motion and the first eigenfrequency of the blade. This way of incorporating couplings between the different modes for energy transfer is therefore not sufficient and other methods where the truncated modes are included

should be investigated e.g. by use of nonlinear normal modes.

However, for normal operation of the wind turbine outside the resonance peaks the two models perform very similar when the number of modes are four but even three modes should produce almost identical results reducing the computational cost.

Acknowledgements

References

Apiwattanalunggarn, P., Shaw, S.W., Pierre, C. and Jiang, D. (2003), "Finite-element-based nonlinear modal reduction of a rotation beam with large-amplitude motion", *J. Vib. Control*, **9**, 235-263.

Baker, C.P., Genaux, M.E. and Burton, T.D. (1993), "Experimental study of chaos in a flexible parametrically excited beam", *Dyn. Vib. Time-Varying Syst. Struct.*, **56**, 195-206.

Behdinan, K., Stylianou, M.C. and Tabarrok, B. (1998), "Co-rotational dynamic analysis of flexible beams", *Comput. Method. Appl. M.*, **154**, 151-161.

Crisfield, M.A. (1990), "A consistent co-rotational formulation for non-linear, three-dimensional, beam-elements", *Comput. Method. Appl. M.*, **81**, 131-150.

Crisfield, M.A., Galvanetto, U. and Jelenić, G. (1997), "Dynamics of 3-D co-rotational beams", *Comput. Mech.*, **20**, 507-519.

Martin O.L. Hansen (2000), *Aerodynamics of Wind Turbines*, James & James (Science Publishers) Ltd.

Steen Krenk (2005), "Non-linear modelling and analysis of structures and solids", Lecture notes. Department of Mechanical Engineering, Technical University of Denmark.

Larsen, J.W. and Nielsen, S.R.K. (2006a), "Non-linear dynamics of wind turbine wings", *J. Non-Linear Mech.*, **41**, 629-643.

Larsen, J.W. and Nielsen, S.R.K. (2006b), "Nonlinear parametric instability of wind turbine wings", *J. Sound Vib.*, (in press.)

Hsiao, K.M., Lin, J.Y. and Lin, W.Y. (1999), "A consistent co-rotational finite element formulation for geometrically nonlinear dynamic analysis of 3-D beams", *Comput. Method. Appl. M.*, **169**, 1-18.

Nayfeh, A.H., Chin, C. and Nayfeh, S.A. (1995), "Nonlinear normal modes of a cantilever beam", *J. Vib. Acoustics*, **117**, 417-481.

Sandhu, J.S., Stevens, K.A. and Davies, G.A.O. (1990), "A 3-D, co-rotational, curved and twisted beam element", *Comput. Struct.*, **35**(1), 69-79.

Volovoi, V.V., Hodges, D.H., Cesnik, C.E.S. and Popescu, B. (2001), "Assessment of beam modeling methods for rotor blade applications", *Math. Comput. Model.*, **33**, 1099-1112.

Wolf, A., Swift, J.B., Swinney, H.L. and Vastano, J.A. (1984), "Determining lyapunov exponents from a time series", *Physica*, **16D**, 285-317.

Yu, W., Hodges, D.H., Volovoi, V. and Cesnik, C.E.S. (2002), "On timoshenko-like modelling of initially curved and twisted composite beams", *J. Solids Struct.*, **39**, 5101-5121.

Appendix A. TIme dependent coupling coefficients

In this appendix the time dependent coupling coefficients i.e., $k_{ij}(t)$, $c_{ij}(t)$, $a_{ijk}(t)$, $b_{ijk}(t)$ and $f_i(t)$ are rewritten into as many time independent terms as possible to gain a more optimized code. The aerodynamic load is also described.

Inserting the relevant components of $\underline{D}(t)$ and $\underline{\underline{E}}(t)$ as given by Eq. (12) and Eq. (11), respectively, and the local components of the support point motions given by Eq. (6), the time dependent coefficients Eq. (10) and Eq. (14) may be written in the following way

$$k_{ij}(t) = -k_{ij,11}\Theta_{2,0}^2\dot{u}^2(t) + k_{ij,12}\Theta_{2,0}(\ddot{u}(t)\sin\Omega_0 t + \dot{u}(t)\Omega_0\cos\Omega_0 t)$$

$$+ k_{ij,21}\Theta_{2,0}(-\ddot{u}(t)\sin\Omega_0 t + \dot{u}(t)\Omega_0\cos\Omega_0 t)$$

$$+ k_{ij,22}((-\Theta_{2,0}^2\dot{u}^2(t)\sin^2\Omega_0 t - \Omega_0^2) + k_{ij,33}(\Theta_{2,0}^2\dot{u}^2(t)\cos^2\Omega_0 t + \Omega_0^2))$$

$$c_{ij}(t) = -c_{ij,1}\dot{u}(t)\Theta_{2,0}\sin\Omega_0 t$$

$$a_{ijk}(t) = a_{ijk,0}(t) - a_{ijk,1}\Theta_{2,0}(\ddot{u}(t)\cos\Omega_0 t + \dot{u}(t)\Omega_0\sin\Omega_0 t) - a_{ijk,2}\Theta_{2,0}^2\dot{u}^2(t)\sin\Omega_0 t\cos\Omega_0 t$$

$$b_{ijk}(t) = -b_{ijk,1}\Theta_{2,0}\dot{u}(t)\cos\Omega_0 t + b_{ijk,2}\Omega_0$$

$$f_i(t) = f_{i,0}(t) + f_{i,1}\Theta_{2,0}(\ddot{u}(t)\cos\Omega_0 t - \Omega_0\dot{u}(t)\sin\Omega_0 t) - f_{i,2}\Theta_{2,0}^2\dot{u}^2(t)\sin\Omega_0 t\cos\Omega_0 t + f_{i,3}\ddot{u}(t) \tag{19}$$

where the time independent coefficients are found to be

$$c_{ij,1} = 2\int_0^L \mu(-\Phi_1^{(i)}\Phi_2^{(j)} + \Phi_2^{(i)}\Phi_1^{(j)})dx_3'$$

$$k_{ij,\alpha\beta} = \int_0^L \mu\Phi_\alpha^{(i)}\Phi_\beta^{(j)}dx_3', \quad k_{ij,33} = \int_0^L \left[\frac{\partial\Phi_\alpha^{(i)}}{\partial x_3'}\frac{\partial\Phi_\alpha^{(j)}}{\partial x_3'}\Big|_{x_3'}^L \mu x_3' dx_3'\right]dx_3'$$

$$a_{ijk,0} = \int_0^L \left[\frac{\partial\Phi_\alpha^{(i)}}{\partial x_3'}\frac{\partial\Phi_\alpha^{(j)}}{\partial x_3'}\Big|_{x_3'}^L - p_{\beta,A}''\frac{\partial\Phi_\beta^{(k)}}{\partial x_3'}dx_3' + \frac{1}{2}\Phi_\alpha^{(i)}p_{\beta,A}''\frac{\partial\Phi_\alpha^{(j)}}{\partial x_3'}\frac{\partial\Phi_\beta^{(k)}}{\partial x_3'}\right]dx_3'$$

$$a_{ijk,\alpha} = \int_0^L \left[\frac{\partial\Phi_\beta^{(i)}}{\partial x_3'}\frac{\partial\Phi_\beta^{(j)}}{\partial x_3'}\Big|_{x_3'}^L - \mu\Phi_\alpha^{(k)}dx_3'\right]dx_3', \quad b_{ijk,\alpha} = 2a_{ijk,\alpha}$$

$$f_{i,0} = \int_0^L \Phi_\alpha^{(i)}p_{\alpha,A}''dx_3', \quad f_{i,\alpha} = -\int_0^L \Phi_\alpha^{(i)}\mu x_3'dx_3', \quad f_{i,3} = \int_0^L \Phi_1^{(i)}\mu dx_3' \tag{20}$$

Appendix B. Aerodynamic load

The incoming wind velocity $V_1'(x_3', t)$ as seen from a considered cross section of the blade varies periodically with the rotational speed Ω_0. $V_1'(x_3', t)$ is assumed to vary logarithmic in the following way

$$V_1'(x_3', t) = V_0\frac{\ln x_3}{\ln h} = V_0\frac{\ln(h - x_3'\cos\Omega_0 t)}{\ln h} \tag{21}$$

where V_0 is the undisturbed mean wind velocity and h is the height of the rotor axis. The rotational wind velocity is given as $V_2'(x_3') = x_3'\Omega_0$. Then, the resulting wind velocity $V(x_3', t)$ may be written as

$$V(x_3', t) = \sqrt{V_1'^2(x_3', t) + V_2'^2(x_3')} \tag{22}$$

The following expression for the aerodynamic loads are used

$$p_{1,A}''(x_3', t) = \frac{1}{2}\rho V^2(x_3', t)c(x_3')c_L \simeq p_{1,A,0}''(x_3') + \Delta p_{1,A,1}''(x_3')\cos\Omega_0 t$$

$$p_{2,A}''(x_3', t) = \frac{1}{2}\rho V^2(x_3', t)c(x_3')c_D \simeq p_{2,A,0}''(x_3') + \Delta p_{2,A,1}''(x_3')\cos\Omega_0 t \tag{23}$$

where ρ is the density of air, V is the resulting wind velocity from the incoming wind velocity and the rotational wind velocity, c is the chord length, and c_L and c_D are the lift and drag coefficients, respectively. In the simulations the following values are used: $V_0 = 15$ m/s, $h = 60$ m, $\rho = 1.2$ kg/m^3, $c_L = 1.5$ and $c_D = 0.05$. $p''_{\alpha,A,0}(x_3')$ denotes the mean value of $p''_{\alpha,A}(x_3', t)$, when the blade is at the top and bottom positions. Correspondingly, $\Delta p''_{\alpha,A,1}(x_3')$ denotes half of the difference between these extreme values. The coefficients $a_{ijk,0}(t)$ and $f_{i,0}(t)$ in Eq. (20) may then be written in the following way

$$a_{ijk,0}(t) = a_{ijk,00} + \Delta a_{ijk,01}\cos\Omega_0 t, \quad f_{i,0}(t) = f_{i,00} + \Delta f_{i,01}\cos\Omega_0 t \qquad (24)$$

with

$$a_{ijk,00} = \int_0^L \left[\frac{\partial \Phi_\alpha^{(i)}}{\partial x_3'}\frac{\partial \Phi_\alpha^{(j)}}{\partial x_3'}\int_{x_3'}^L \left[-p''_{\beta,A,0}\frac{\partial \Phi_\beta^{(k)}}{\partial x_3'}\right]dx_3' + \frac{1}{2}\Phi_\alpha^{(i)} p''_{\beta,A,0}\frac{\partial \Phi_\alpha^{(j)}}{\partial x_3'}\frac{\partial \Phi_\beta^{(k)}}{\partial x_3'}\right]dx_3'$$

$$\Delta a_{ijk,01} = \int_0^L \left[\frac{\partial \Phi_\alpha^{(i)}}{\partial x_3'}\frac{\partial \Phi_\alpha^{(j)}}{\partial x_3'}\int_{x_3'}^L \left[-\Delta p''_{\beta,A,1}\frac{\partial \Phi_\beta^{(k)}}{\partial x_3'}\right]dx_3' + \frac{1}{2}\Phi_\alpha^{(i)}\Delta p''_{\beta,A,1}\frac{\partial \Phi_\alpha^{(j)}}{\partial x_3'}\frac{\partial \Phi_\beta^{(k)}}{\partial x_3'}\right]dx_3'$$

$$f_{i,00} = \int_0^L \Phi_\alpha^{(i)} p''_{\alpha,A,0}\,dx_3', \quad \Delta f_{i,01} = \int_0^L \Phi_\alpha^{(i)}\Delta p''_{\alpha,A,1}\,dx_3'$$

Appendix C. Specifications of blade

The theory is demonstrated using a 46 m pitch regulated blade. The aerodynamic profiles are NACA 63-418 section profiles as illustrated in Fig. 9, scaled with chord and height values indicated in Fig. 11(d). The inner 2.0 m of the blade has a circular cross section with a diameter of 2.0 m. In Fig. 10 the blade is shown based on the geometry of the root and the scaling and pretwisting of the NACA 63-418 profile. The blade has the pretwist angle, the mass, local moments of inertia, chord length and thickness distributions as indicated in Fig. 11. The total weight is 10 t. The stiffness and mass distribution are chosen so that the eigenfrequencies approximately match those given by a manufacture of a corresponding blade size. The modulus of elasticity is $E = 3 \cdot 10^4$ MPa. The twist throughout the blade is chosen so that the angle of attack of the resulting wind is approximately 6° at a constant rotational speed of 1.6 rad/s, and an incoming wind velocity of 12 m/s. At these nominal values a wind turbine with such three blades should produce approximately 2.75 MW according to the Blade Element Momentum theory described in Hansen 2000.
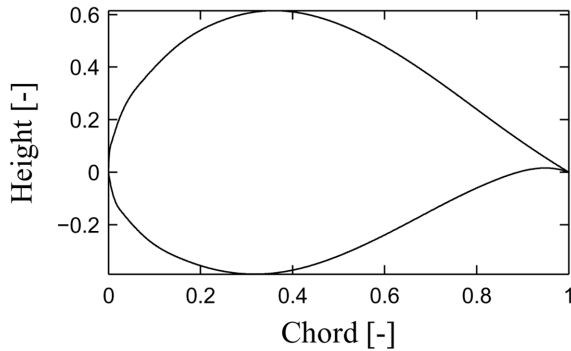

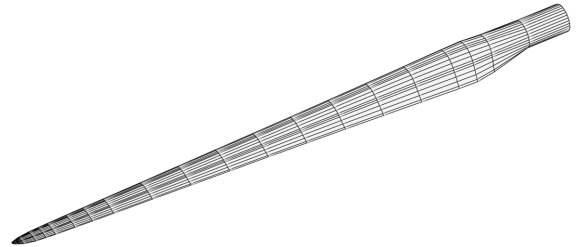Fig. 9 Normalized profile of a NACA 63-418 blade section

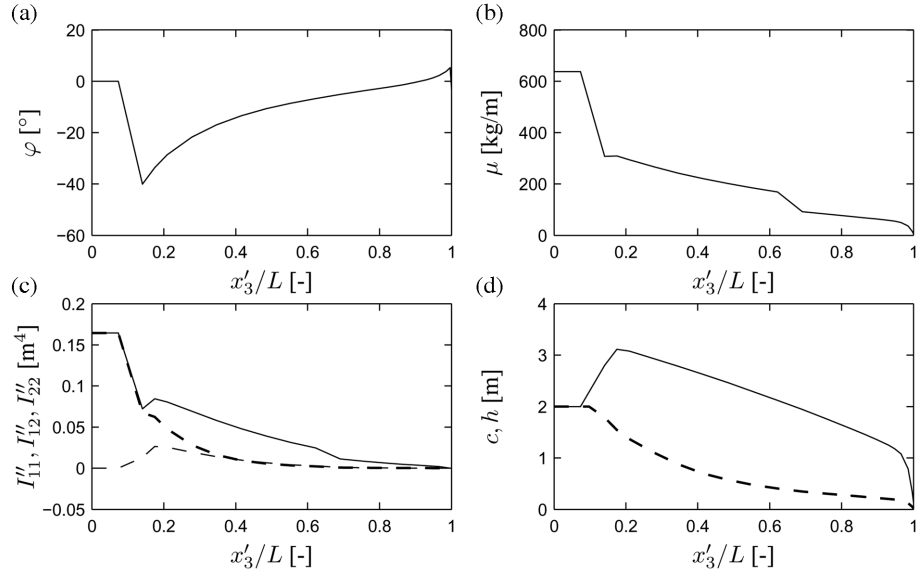Fig. 10 Illustration of the used blade in the simulations

Fig. 11 (a) Pretwist angle throughout the beam, (b) Mass per unit length, (c) Distribution of local moment of inertia. (—) I_{11}'' . (– –) I_{12}'' . (– –) I_{22}'' . (d) (—) Chord length c. (– –) Height h of cross sections